

Single and biphoton imaging and high dimensional quantum communication

John C. Howell · Petr M. Anisimov ·
Jonathan P. Dowling · Robert W. Boyd

Received: 2 May 2011 / Accepted: 24 August 2011 / Published online: 30 October 2011
© Springer Science+Business Media, LLC 2011

Abstract Here, we present recent developments in the field of quantum imaging focusing on the high dimensionality aspects of single and biphoton imaging. We discuss some systems that have a “quantum advantage” over classical counterparts. We highlight some recent experiments in single-photon image discrimination, large alphabet quantum key distribution and image buffering.

Keywords Quantum optics · Quantum communication · Quantum imaging · Slow light · Entangled photons

1 Introduction

Quantum information science has made great strides over the last two decades. Motivated by technologies that cannot be replicated classically, such as provably secure communication [1–3] and factoring large numbers into their primes [4] with the use of quantum computers [5–8], there has been great interest in determining those systems where there is a “quantum advantage”. Researchers in the field of quantum imaging have sought to determine those advantages for imaging (see for example the review by Kolobov [9]). While the field of quantum imaging has many subfields, this review

J. C. Howell (✉) · R. W. Boyd
Department of Physics and Astronomy, University of Rochester, Rochester, NY 14627, USA
e-mail: howell@pas.rochester.edu

P. M. Anisimov · J. P. Dowling
Hearne Institute for Theoretical Physics, Department of Physics and Astronomy,
Louisiana State University, Baton Rouge, LA 70803, USA

R. W. Boyd
Institute of Optics, University of Rochester, Rochester, NY 14627, USA

will focus on imaging with single photons or biphotons. Further, the high information capacity of the single and biphotons will be shown to be useful in increasing the information capacity of a quantum key distribution system.

“Single photon imaging” almost sounds like an oxymoron. How can a single photon carry an image and even if it can, how can it be measured? Quantization of the electromagnetic field shows that the elementary unit of energy, “the photon,” can have infinite information capacity at zero temperature (no thermal noise photons [10]). However, for fundamental and practical reasons, the amount of information that can be extracted from the photon has usually been limited to much less than a bit, let alone the Mona Lisa. From a fundamental perspective, the space-time modes of the quantization are not usually related to the space-time characteristics of a detector used to measure the photons. For example, the plane-wave decomposition of the field is a useful mathematical construct, but it not possible to measure. However, if one possessed a detector that could detect all plane-wave modes, the photon, even if it occupied all modes, would only be measured in a single eigenmode of that detector. It would then require an ensemble of identical photons to determine a single photon’s state. The implication is that an infinite number of photons are needed to determine the image written on the photon. We see then that we must use nonstandard methods for determining single photon images, as well we must ascertain the advantages of single photon imaging versus traditional classical methods.

Claude Shannon’s discussion of information theory [11] gives us a theoretical framework with which to study the image or information capacity of a single photon. Shannon showed that the entropy is a direct measure of information. Consider an idealized detector with unit quantum efficiency, 100% fill factor and a square 2-D array of form factor 1 cm^2 with square pixels roughly equal in size to a photon at the diffraction limit ($\approx 1 \mu\text{m}^2$). Let us also assume that a photon has a uniformly distributed probability distribution over the detector array (i.e., it is equally likely to be measured by any of the pixels). The quantum entropy is then $S = -\text{Tr}[\rho \log_2 \rho] = -\sum_{i,j} p_{ij} \log_2 p_{ij}$, where $p_{ij} = \frac{1}{N^2}$ is the probability of finding the photon in the i^{th} column and j^{th} row pixel of the detector and ρ is the density matrix for the photon. Using the numbers just described, the quantum entropy is 26.6 or equivalently the photon has a measurable capacity of approximately 27 bits in the transverse degree of freedom. In other words, excluding the time and frequency domains, the transverse single photon image for the idealized detector of standard form factor has an upper limit of about 27 bits worth of measurable information. If the detector has far fewer pixels (e.g., a 32×32 single photon avalanche pixel array corresponding to 10 bits), the entropy is greatly reduced. This context-dependent entropy determined by the detector, places an upper limit on the measurable transverse information capacity of the system, regardless of the photon’s actual information content. Unfortunately, once again, even though there are potentially 27 bits worth of measurable information, we cannot determine the transverse profile of the photon in a single measurement using this traditional technique. To determine the image, we must integrate over a large number of events before we it is possible determine the transverse profile of the photon. On the other hand, it is this uncertainty that leads to the possibility of having very large alphabets in

quantum communication. In other words, it is possible to have up to 27 bits of usable information per photon for quantum communication purposes.

Much of quantum information has focused on the spin-like behavior of two-level systems such as the polarization states of a photon. However, as shown above, the dimensionality of the vector spaces can be much larger. An important example [12–14] is the use of the orbital angular momentum states, such as Laguerre-Gauss modes. They form an infinite basis owing to the fact that angular momentum has no upper bound, implying there is no limit to the information content that can be carried by a single photon. Other examples of the large information content of quantum light fields exist as well [15–18]. Moreover, it has recently been shown that the entanglement between two photons generated by the process of parametric down conversion can exist in a high-dimensional Hilbert space; entanglement between two qudits was demonstrated for both $d = 3$ and $d = 6$ with transverse position-momentum entangled biphotons [19], and $d = 1024$ with energy-time entangled biphotons [20].

In this brief review, we will discuss techniques for extracting the image encoded on a single photon in Sect. 2, consider a high dimensional quantum key distribution scheme in Sect. 3 and discuss a quantum buffer for single photon images in Sect. 4.

2 Single photon image discrimination

We have seen that a 2-D array of photon counters used for extracting an image from a single photon bears little fruit. However, using holographic matched filtering it is possible to determine the image encoded on a photon in a single or very few measurement events. Matched filtering is a powerful method for improving the information readout in detection. It was first developed to optimize the signal to noise ratio for a signal in a noisy background [21]. A filter is considered to be matched when its impulse response $h(x, y)$ is given by $s^*(-x, -y)$ for an input signal $s(x, y)$. The filter maximizes the cross-correlation

$$|h(x, y) \star s(x, y)|, \quad (1)$$

where \star denotes convolution [22]. Optically, such a filter can be realized using the Vander Lugt optical correlator [23]. A Vander Lugt correlator consists of three planes of interest (P1, P2 and P3) and two lenses each of focal length f . The planes P1 and P2 are separated by $2f$ with a lens placed at the midpoint. The same relationships hold for planes P2 and P3 and the second lens. The lenses give scaled Fourier transforms of the fields in P1 and P2 in planes P2 and P3, respectively. A matched filter is placed in plane P2. The optical correlator behaves as follows. A signal with transverse spatial pattern $s(x, y)$ is found in P1. In P2, we have a scaled Fourier transform of the signal $S(f_x, f_y)$, which passes through the filter with transfer function $H(f_x, f_y)e^{-if_y k_1}$. Immediately after P2, the field is given by

$$U_2(f_x, f_y) = S(f_x, f_y)H(f_x, f_y)e^{-if_y k_1}. \quad (2)$$

Since the Fourier transform of the product of two functions is the convolution of the Fourier transforms, P3 gives the squared modulus of the cross-correlation pattern of the signal with the filter impulse response, thus obtaining the desired matched filter. The phase term $e^{-if_y k_1}$ is used to give a correlation spot in P3 displaced from the origin. When $H(f_x, f_y) = S^*(f_x, f_y)$, it can be seen that the resultant field from P2 is a plane wave, which leads to a small correlation spot in P3. If the filter’s transfer function differs from $S^*(f_x, f_y)$, the correlation spot reduces from its peak value and broadens. In this context, the input signal is the single photon image. If the correlator is matched to the photon image, there is a high probability that the photon will be deflected to the correlation spot corresponding to that image.

The Vander Lugt optical correlator can be improved in several ways. Horner showed that a phase-only filter can increase the Horner efficiency (the amount of light in the correlation spot versus the input signal light) and improve the discrimination [24]. A phase-only hologram eliminates the amplitude component of the transfer function and only keeps the phase. The discrimination efficiency can be further improved by eliminating the low spatial frequency components (high-pass filter) by blocking the low spatial frequencies in the filter (e.g., by overexposing a hologram).

To gain a better understanding of single-photon image discrimination, we will put image discrimination and matched filtering in a quantum mechanical formalism. Quantum mechanically, the ability to discriminate between single-photon images can be accomplished with a suitable basis transformation. We represent the i th single-photon image by

$$|\varphi_i\rangle = \int d\mathbf{x} \varphi_i(\mathbf{x})|1_{\mathbf{x}}\rangle \tag{3}$$

where $|1_{\mathbf{x}}\rangle = \frac{1}{(2\pi)^2} \int d\mathbf{k} e^{i\mathbf{k}\cdot\mathbf{x}}|1_{\mathbf{k}}\rangle$. $|1_{\mathbf{k}}\rangle = \hat{a}_{\mathbf{k}}^\dagger|0\rangle$ is a single-photon Fock state in the \mathbf{k} th mode. An operator of the form

$$\hat{M} = \sum_i |1_{\mathbf{k}_i}\rangle\langle\varphi_i| \tag{4}$$

will transform the i th image into the \mathbf{k}_i th mode for detection as long as

$$\langle\varphi_i|\varphi_j\rangle = \delta_{ij} \tag{5}$$

for all images. Detection of a photon in the plane-wave mode uniquely determines the detected image. Equation (3–5) represent orthogonal state discrimination for single-photon images.

Implementing the transformation of Eq. (4) in the laboratory is fairly difficult, but may be approximated reasonably well with holograms. For thin multiplexed holograms exposed sequentially with object and reference fields of the form $o_i(\mathbf{x}) = A_i(\mathbf{x}) \exp[-i\phi_i(\mathbf{x})] + c.c.$, and $r_i(\mathbf{x}) = r \exp[i\mathbf{k}_i \cdot \mathbf{x}]$, where $A_i(x)$ ($\phi_i(x)$) is the transverse amplitude (phase) function, the hologram has a transmission function of the form,

$$t(\mathbf{x}) = \beta \sum_i T_i |r_i(\mathbf{x}) + o_i(\mathbf{x})|^2 \quad (6)$$

$$= t_0(\mathbf{x}) + \beta \sum_i T_i r A_i(\mathbf{x}) \left[e^{i(\phi_i(\mathbf{x}) + \mathbf{k}_i \cdot \mathbf{x})} + c.c. \right] \quad (7)$$

Here we have taken r , A_i , and ϕ_i to be real. $t_0(\mathbf{x})$ contains all the terms that are not diffracted into any of the $\pm \mathbf{k}_i$ directions, β is a material dependent exposure parameter, and T_i is the exposure time for the i th object/reference pair. Illuminating the developed hologram with the j th image diffracts a portion of the field into the positive \mathbf{k}_i directions,

$$u_j(\mathbf{x}) = \beta \sum_i T_i r A_j(\mathbf{x}) A_i(\mathbf{x}) e^{i(\phi_j(\mathbf{x}) + \phi_i(\mathbf{x}) + \mathbf{k}_i \cdot \mathbf{x})}. \quad (8)$$

If

$$A_j(\mathbf{x}) A_i(\mathbf{x}) = \delta_{ij} A_i^2(\mathbf{x}) \quad (9)$$

then $u_j(\mathbf{x})$ does not contain any field amplitude which is diffracted in the $+\mathbf{k}_{i \neq j}$ direction. As long as the spatial bandwidth of the j th object is much smaller than the separation of the reference modes, $\mathbf{k}_j - \mathbf{k}_{i \neq j}$, the light in the vicinity of the \mathbf{k}_j^{th} mode can be collected and detected, uniquely identifying the image.

Broadbent et al. [25] and Malik et al. [26] recently demonstrated single-photon discrimination using matched-filtered holograms. They showed that if an image is a member of a pre-established basis set, it is possible to determine which image is carried by the photon by passing the photon through a hologram matched to the image. This procedure should be contrasted with the earlier work (e.g., [27]), in which an image was impressed upon a single-photon, but the image was read out in a statistical fashion, one pixel at a time, and thus required an ensemble of events to reproduce the image. That work also established that the individual photons carrying the image could be delayed significantly by passing them through a highly dispersive (slow-light) medium without destroying the image content of the photon.

The basic idea of the Broadbent et al. [25] and Malik et al. [26] work is illustrated in Fig. 1. A multiple-exposure hologram is formed (parts a and b) using two different transmission objects with reference beams applied from different directions. A single photon (part c) passes through one of the two objects and allow it to fall onto the hologram constructed by the procedure shown in parts (a) and (b). This photon will then diffract into one of two output directions depending upon which image was impressed onto the photon. This procedure is well known in optical information processing [28, 29], is related to the more general method of matched filtering [21]. The general methods used in classical image discrimination apply equally well to quantum mechanical light fields. Whereas [12] used simplex holograms to measure single-photon orbital angular momentum states, the present work demonstrates that arbitrary image states from a known basis set may be distinguished by performing a single measure with a multiplexed hologram. In the conceptual example shown in Fig. 1, the basis set consists of only two images. The experimental results demonstrate

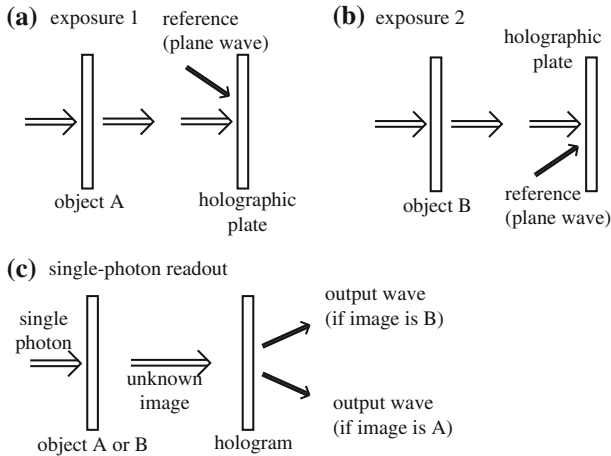


Fig. 1 Concept of the experiment. A multiple-exposure hologram (shown for two exposures) is formed as shown in parts (a) and (b) of the figure. **c** An image is impressed onto a single-photon and the form of the image is determined by diffraction from the hologram

proof-of-principle experiments which distinguish between 2 or 4 orthogonal images. However, much larger sets of images (orthogonal or nonorthogonal) can be used. In the classical field of matched filtering, as many as 10,000 images have been exposed onto a single hologram [30].

A schematic of the Broadbent et al. [25] experimental setup is shown in Fig. 2. Part (a) shows the setup for writing the hologram and part (b) shows the setup for the single-photon readout. For this experiment, stencils of the yin and yang symbol as objects A and B respectively were chosen because of their vanishing spatial overlap. The hologram is a thick angularly multiplexed, phase transmission hologram and is made using PFG-01, a fine-grained red-sensitive silver halide emulsion on a glass plate substrate. The emulsion has a peak light sensitivity of about $100 \mu\text{J}/\text{cm}^2$ at 630 nm.

A HeNe laser ($\lambda = 632 \text{ nm}$) was used as the light source for recording the holograms. The HeNe laser is split at a non-polarizing beamsplitter (NPBS) into object and reference beams. Each beam has a power of $\sim 300 \mu\text{W}$ after the NPBS. The object beam passes through the object stencil and is imaged onto the hologram recording medium with a 50 mm focal length lens, along with one of the two reference beams. A precision translation stage allows us to reproducibly place either object A or B in the object plane. The reference beam is sent to a mirror mounted on a rotation stage which sets the direction of the reference beam. During the exposure, object A (B) is illuminated and the hologram is exposed with reference beam A (B) for 350 ms as set by an electronically controlled shutter.

The characterization of the holograms is as follows. Parts (a) and (b) of Fig. 3 show the quality of the reconstructed images when the hologram is read out by a plane-wave reference beams. Parts (c) and (d) show the diffracted beams when the hologram is illuminated by one of the image-bearing beam. The nature of these results is described by a model of the holographic process. The holographic recording material is illuminated simultaneously by an object wave of field strength $O(\mathbf{x})$ and a reference wave

Fig. 2 Single-photon image-discrimination laboratory setup. **a** Biplex holograms are exposed using a HeNe laser and an electronically controlled shutter. For each exposure a rotation stage selects one of the two reference beams, and a translation stage switches between the two stencils A and B. **b** During the image-discrimination phase of the experiment, heralded single photons are sent through either stencil A or B and are detected at either detector A or B. TCSPC = time-correlated single-photon counter

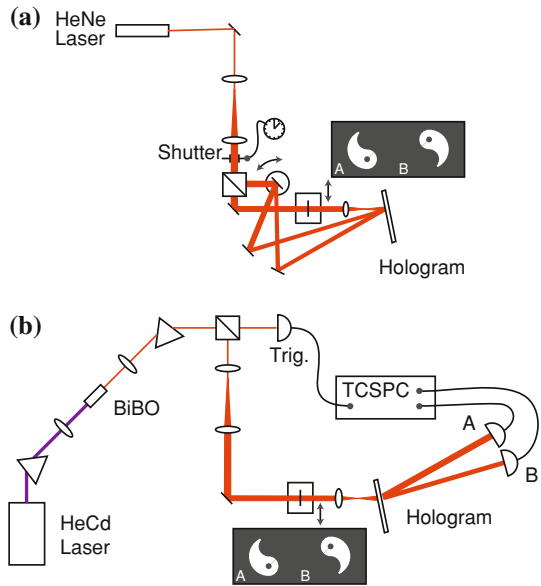
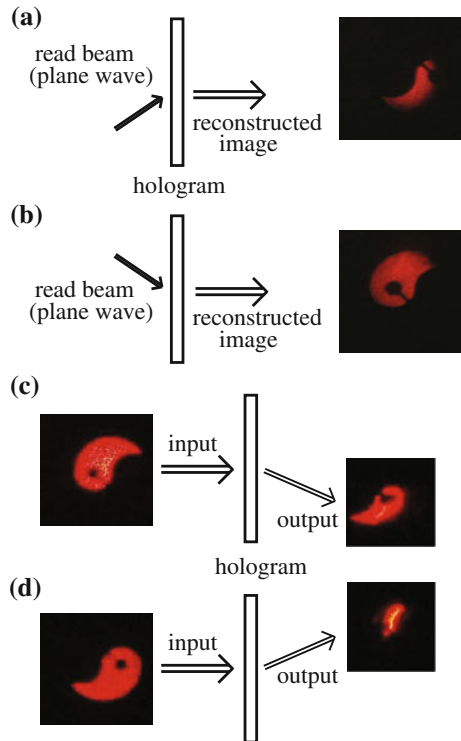


Fig. 3 **a** and **b** Hologram readout for a plane-wave read beam. **c** and **d** Hologram readout with an image-carrying read beam



of field strength $R(\mathbf{x})$ so that the total field at the hologram is $E(\mathbf{x}) = O(\mathbf{x}) + R(\mathbf{x})$. After development, the transmission $t(\mathbf{x})$ of the hologram is proportional to the local optical intensity, so that $t(\mathbf{x}) \propto |O(\mathbf{x}) + R(\mathbf{x})|^2$ or that

$$t(\mathbf{x}) \propto |O(\mathbf{x})|^2 + |R(\mathbf{x})|^2 + O(\mathbf{x})R^*(\mathbf{x}) + O^*(\mathbf{x})R(\mathbf{x}). \quad (10)$$

In the conventional holographic reconstruction process, the hologram is illuminated with a wave identical to the reference wave $R(\mathbf{x})$ used in writing the hologram so that the field leaving the hologram is given by $E_{\text{out}}(\mathbf{x}) \propto R(\mathbf{x})t(\mathbf{x})$ or by

$$R(\mathbf{x})|O(\mathbf{x})|^2 + R(\mathbf{x})|R(\mathbf{x})|^2 + O(\mathbf{x})|R(\mathbf{x})|^2 + O^*(\mathbf{x})R^2(\mathbf{x}). \quad (11)$$

The third term in this expression is the one leading to standard holographic reconstruction, and if $R(\mathbf{x})$ is nearly uniform across the aperture of the hologram we see that this term just reproduces the amplitude distribution $O(\mathbf{x})$ of the original object. Such behavior can be seen in parts (a) and (b) of Fig. 3, where the reconstructed images are accurate replicas of the stencil objects. If, however, the hologram is illuminated by a replica of the structured object beam $O(\mathbf{x})$, as in the case of holographic matched filtering, the situation is more complicated. It is found that $E_{\text{out}}(\mathbf{x}) \propto O(\mathbf{x})t(\mathbf{x})$ or by

$$O(\mathbf{x})|O(\mathbf{x})|^2 + O(\mathbf{x})|R(\mathbf{x})|^2 + O^2(\mathbf{x})R^*(\mathbf{x}) + |O(\mathbf{x})|^2R(\mathbf{x}) \quad (12)$$

In this case, the fourth term is the one leading to the diffracted output beam implying the transverse structure of the object beam will be imprinted onto the diffracted beam. This behavior is apparent in the data shown in parts (c) and (d) of Fig. 3. Quantitatively, a peak diffraction efficiency of about 24% (19%) for objects A (B) is measured, and the cross-talk between them is negligible.

The image-discrimination phase of the experiment is performed with the setup of Fig. 2b. The object beam is created by heralded single photons emitted by spontaneous parametric down conversion (SPDC). A 10-mm-long BiBO crystal cut for collinear type-I phase matching is angle tuned to produce degenerate biphotons at 650 nm. The biphotons are separated from the pump beam and are sent to a nonpolarizing beam splitter (NPBS). One output port of the NPBS is coupled directly through a multimode optical fiber to a photon detector which serves as a trigger, heralding the presence of a photon, hereafter called the image photon, in the other output port. The image photon passes through the stencil and hologram along the same path as when the hologram was exposed. After diffracting from the hologram, the image photons are coupled through multimode fibers to detectors A or B. All three detectors used in the experiment are Perkin Elmer single-photon counting module (SPCM) detectors. Detection events are counted with a PicoQuant PicoHarp 300, a time-correlated single-photon counter (TCSPC).

When stencil A (B) is used as the object, the image-discrimination photons are diffracted by the hologram into the direction of reference beam A (B). Coincidences between the heralding photons and the image-discrimination photons are measured for the four object–detector combinations: (1) A–A, (2) A–B, (3) B–A, and (4) B–B. The total number of coincidences for 54 min of integration are reported in Table 1.

Table 1 Image-discrimination results showing the total number of raw coincidences (C), accidental coincidences (A), and C/A ratio for each object–detector combination. Also shown are the heralding photon and image discrimination photon singles rates, s_h and s_{id} . Background rates are $b_h \simeq 1000 \pm 32$ Hz, $b_{id,A} = 420 \pm 20$ Hz, and $b_{id,B} = 249 \pm 16$ Hz. $1/R\Delta t$ represents the maximum possible C/A ratio as discussed in the text

Ob.-Dt.	C	A	C/A	s_h	s_{id}	$1/R\Delta t$
A-A	5738 ± 75	337 ± 18	16.99 ± 0.95	437 kHz	473 Hz	143 ± 3
A-B	185 ± 14	201 ± 14	0.93 ± 0.09	522 kHz	252 Hz	N/A
B-A	289 ± 17	287 ± 17	1.01 ± 0.08	444 kHz	414 Hz	N/A
B-B	4401 ± 66	229 ± 15	19.24 ± 1.30	511 kHz	273 Hz	210 ± 5

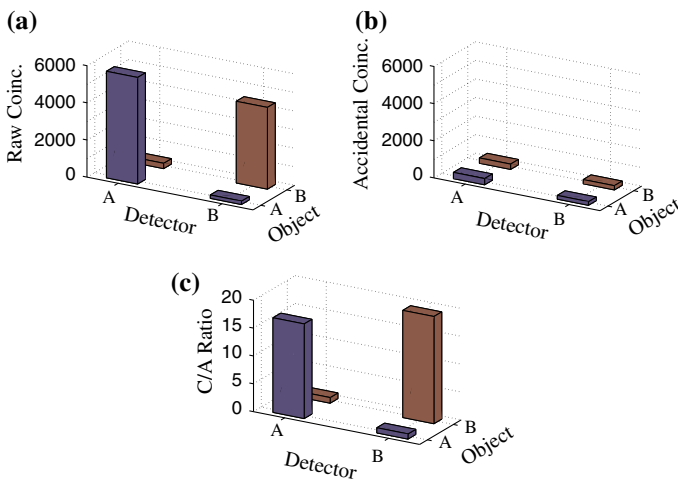


Fig. 4 Graphical display of image-discrimination results. Total number of raw coincidences (C), accidental coincidences (A), and C/A ratio for each object–detector combination

For better visualization, these results are also shown graphically in Fig. 4. Raw coincidences are the number of coincident events generated within the 500 ps coincidence window. Coincident events arise from coincidences between the herald/image-discrimination photons as well as random coincident events between (a) a background count and a heralding photon, (b) a background count and an image-discrimination photon, (c) two background counts, or (d) two uncorrelated photons from a multi-pair event. By counting the number of image-discrimination photons that arrive 20 ± 0.25 ns after the heralding photons we can measure the number of accidental coincidences arising from events (a)–(d) above. The single-event count rates are ~ 500 k counts per sec for the trigger and ~ 450 counts per sec (~ 250 counts per sec) for detector A (B) (see Table 1). In practice, the high degree of loss in the image-discrimination arm implies that the accidental coincidences are dominated by coincidences between background counts and heralding photons.

The system fidelity can be quantified in terms of the ratio of true coincidences N_{AA} (N_{BB}) to false coincidences N_{AB} (N_{BA}). The ratio $f_A = N_{AA}/N_{AB}$ ($f_B = N_{BB}/N_{BA}$) is found to be 31.2 (15.2), demonstrating that object A can be distinguished from B

with a confidence level of $\sim 96.8\%$ (93.4%). It is evident from the data in Table 1 that nearly all of the false events, N_{AB} and N_{BA} , can be attributed to accidental coincidences (because the C/A ratios for the A–B and B–A object–detector combinations are approximately unity). The system fidelity can therefore be increased by improving the C/A ratios for the A–A and B–B object–detector combinations. The C/A ratios can be improved by increasing the total collection efficiency in the image-discrimination arm or by using detectors with reduced dark counts for the image-discrimination photon. The low collection efficiency in the image-discrimination arm is due to a combination of reflection losses at lenses, mirrors and beamsplitters, transmission losses at the image mask and hologram, coupling losses from coupling a highly multimode image into a multi-mode optical fiber, and alignment issues caused by using different laser wavelengths for the hologram exposure, single-photon generation, and single-photon alignment.

For many applications, a much larger basis set, possibly including non-spatially separated, or more generally, non-orthogonal images, would be desirable. Image discrimination of non-orthogonal images using numerical correlation methods has been investigated by [31] where he showed that distinguishing nearly identical images with a confidence level of 97% requires about 250 photons. For a basis set involving non-orthogonal images the principles of unambiguous state discrimination in large Hilbert spaces [32] may be applied to design a hologram which optimally discriminates images in the basis set. Limits to the number of images that can be discriminated in a hologram are set by issues such as cross talk, which tends to increase with the number of stored images, and diffraction efficiency, which tends to decrease with the number of stored images.

3 Large entropy quantum key distribution from biphotons

As pointed out earlier, a single photon can have very high entropy. The entropy is the measure of usable information in the photon. Essentially, it is a measure of the uncertainty of where and when the photon will be measured. This uncertainty can be exploited for secure quantum communication. For polarization states, the maximum entropy of a single photon corresponds to a single bit, since there are two possible outcomes. However, we can explore the much larger dimensional spaces of the transverse or longitudinal domains. We can make use of this entropy for increasing the dimensionality and ultimately, the information throughput in a quantum key distribution (QKD) scheme.

Quantum key distribution has continued to progress toward the goal of practical and provably secure key distribution operating at high bandwidths and over large distances [33]. Achieving high bandwidths over large distances remains a challenge to researchers, and it is for this reason that recent studies have focused on the possibility of increasing the information content of each transmitted quantum state by using states with higher dimensionality d [12, 15, 17, 19, 34, 35], i.e. qudits instead of qubits. Higher dimensional quantum states also have the attractive properties of an increased sensitivity to eavesdropping and a decreased sensitivity to noise [36, 37].

Consider the unnormalized biphoton state

$$|\Psi\rangle \propto \int dt_1 dt_2 A(t_1, t_2) B(t_1, t_2) e^{-i \frac{\omega_p}{2} (t_1+t_2)} \hat{a}_1^\dagger(t_1) \hat{a}_2^\dagger(t_2) |0\rangle, \tag{13}$$

where ω_p is the down-conversion pump frequency and $\hat{a}_i^\dagger(t_i)$ is the photon creation operator in mode i at time t_i [38]. After passing through spectral filters, a Gaussian correlation function $A(t_1, t_2) = e^{-\frac{(t_1-t_2)^2}{4\tau^2}}$ provides a good approximation for the biphoton temporal correlation function, where the correlation time τ is on the order of ~ 100 fs, as determined by the 10 nm bandwidth of the spectral filters. The biphoton temporal correlation function $A(t_1, t_2)$ can be understood as the correlation between the time at which the two photons exit the nonlinear crystal. Also, $B(t_1, t_2) = e^{-\frac{(t_1+t_2)^2}{16T^2}}$ represents the biphoton envelope function, where the biphoton envelope T is given by the coherence time of the pump photon of frequency ω_p that was destroyed in the creation of the entangled biphoton. The biphoton coherence time is on the order of ~ 500 ns corresponding to the inverse laser linewidth. For mathematical simplicity it is straightforward to show that for $T \gg \tau$, $A(t_1, t_2)B(t_1, t_2) \simeq e^{-\frac{(t_1-t_2)^2}{4\tau^2}} e^{-\frac{t_1^2}{4T^2}}$. The Schmidt number, or number of information eigenmodes, of Eq. (13) is given by $K \sim T/\tau$ [39,40].

Suppose that a party, Alice, sends another party, Bob, one photon of the entangled state discussed above, and keeps the other photon under her control. Suppose now that an eavesdropper, Eve, makes a positive operator value measurement (POVM) on the arrival time of the photon sent to Bob [41]. We model Eve’s measurement as a projective filter function, $\hat{M}_e = \int dt f(t, T_E) a_e^\dagger(t) |0\rangle \langle 0| a_e(t)$, where $f(t, T_E)$ is a general filter function and T_E is related to the resolution of Eve’s POVM. A gaussian filter function $f(t, T_E) = e^{-\frac{t^2}{4T_E^2}}$ gives

$$|\Psi_M\rangle \propto e^{-\frac{(t_1-t_2)^2}{4\tau^2}} e^{-\frac{t_1^2}{4}\left(\frac{1}{T^2} + \frac{1}{T_E^2}\right)} \hat{a}_1^\dagger(t_1) \hat{a}_2^\dagger(t_2) |0\rangle, \tag{14}$$

which represents the biphoton wavefunction after Eve’s POVM. For $T_E \ll T$ we get $\left(\frac{1}{T^2} + \frac{1}{T_E^2}\right) \sim \frac{1}{T_E^2}$, which gives us $K \sim T_E/\tau$. This implies that Eve’s POVM results in a decrease in the Schmidt number; eavesdropping has decreased the number of information eigenmodes.

It has been shown that the Franson interference visibility [42] can be used as a Bell-type entanglement measure for energy-time entanglement [43,44]. We find that the Franson fringe visibility, along with the known path mismatch, can also be used to measure the biphoton envelope width T (or T_E after Eve’s POVM). If Alice and Bob send the state in Eq. (14) through a Franson interferometer, the post-selected coincidence rate is given by

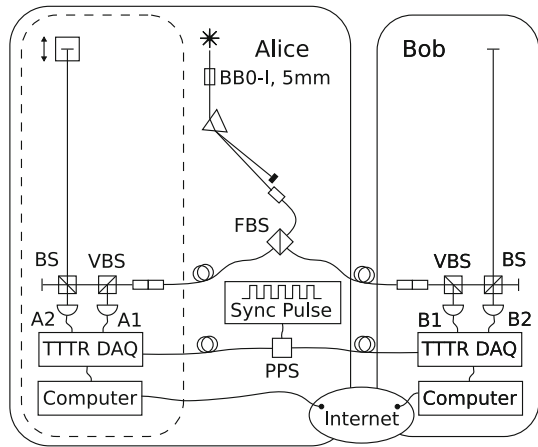
$$R_M \propto \int dt_a dt_b |\langle 0 | \alpha(t_a, t_b, \delta t, \Delta t) | \Psi_M \rangle|^2 \quad (15)$$

$$\cong 1 + \cos \left[\frac{\omega_p}{2} (2\Delta t + \delta t) \right] e^{-\frac{\delta t^2}{8\tau^2}} e^{-\frac{\Delta t^2}{8T_E^2}}, \quad (16)$$

where $\alpha(t_a, t_b, \delta t, \Delta t) = (\hat{a}_1(t_a + \Delta t + \delta t)\hat{a}_2(t_b + \Delta t) + \hat{a}_1(t_a)\hat{a}_2(t_b))$, where $a_{1,2}(t)$ is the destruction operator for Alice's and Bob's detectors respectively, Δt is the path mismatch in Bob's arm of the Franson interferometer, and δt is the difference in path mismatches between Alice's and Bob's arms of the Franson interferometer. A strong drop in Franson fringe visibility is observed when $T_E \lesssim \Delta t$. Therefore we can detect the presence of Eve's POVM by observing a reduction in the visibility of Alice's and Bob's Franson fringes, as predicted by the exponential function in Eq. (16). Note that a larger path mismatch Δt provides a more sensitive test against Eve's POVM.

The energy-time entanglement QKD protocol we present here is accomplished in 6 steps. (1) Alice sends Bob one photon of an energy-time entangled biphoton and keeps one for herself. (2) Alice and Bob randomly and independently measure arrival times of their incoming photon either directly with low-jitter (FWHM ~ 50 ps, $1/e^2$ width ~ 350 ps) detectors (timing detector) or after sending their photon through an unbalanced Michelson interferometer acting as one-half of a Franson interferometer (see Fig. 6). These timing measurements of Alice and Bob are accurately synchronized to each other by using a shared, public, synchronization pulse signal. This sync signal has a period of 64 ns between consecutive pulses in our experiment, where each pulse is measured, counted and recorded. During the entirety of the QKD process Alice privately scans one arm of her unbalanced interferometer between two, neighboring, Franson interference maximum and minimum locations (predetermined during initial calibration). (3) After all the photons have been detected, Bob publicly sends Alice the exact arrival times of the photons that were detected in the output of his Michelson interferometer. Alice uses this information, along with her own Franson timing measurements and respective interferometer scan locations, to determine the visibility of the Franson fringes. (4) Using the measured visibility, Alice determines the security of the system and communicates the status of security to Bob. If the system is measured to be secure then Alice and Bob can proceed with the QKD protocol. (5) Alice and Bob privately bin their remaining (non-Franson) timing measurements, where each bin corresponds to a character of the QKD alphabet (see Fig. 7). Details of the binning procedure are explained below. For our experiment the bin size, σ , is varied between 48 ps–30.6 ns, where a tradeoff between alphabet size and BER is explored. The first bin of the alphabet begins with each sync pulse, and the alphabet extends over the period of the sync signal (64 ns for our experiment). (6) Alice and Bob publicly publish the relevant sync periods in which they measure the arrival of non-Franson photons, however they keep the precise binning information from step (5) private. Alice and Bob discard the non-Franson photon arrival events that do not occur in the same sync periods, and keep the rest. Alice and Bob are thus left with identical photon events, where both photons of a downconversion pair are measured in the same time bin by Alice and Bob. The unpublished,

Fig. 5 Experimental Setup. BS, FBS, VBS, and PPS, refer to a 50:50 beamsplitter, a fiber 50:50 beamsplitter, a variable beamsplitter made with a half wave plate and a polarizing beam splitter, and a passive power splitter, respectively



precise arrival times for the accepted photon detection events thus give Alice and Bob a common key.

An outline of the experiment is shown in Fig. (5). Alice uses a 50 mW, 390 nm, cw laser having a bandwidth of 2 MHz to pump 5 mm of BBO-I cut for collinear, degenerate downconversion (with measured raw singles rate ~ 800 KHz and coincidence rate ~ 60 KHz using PerkinElmer SPAD with single mode fiber). The downconverted photons are coupled into a singlemode, 50:50, fiber beamsplitter, where one photon is sent to Alice and the other to Bob. The instances where both photons travel to either Alice or Bob can presently be ignored. Using a variable beamsplitter, Alice and Bob randomly and independently send their photons either to a high resolution timing detector (A1/B1; MPD PMD; background dark-count rate ~ 250 Hz; background light-count rate ~ 1 KHz; singles rate ~ 20 KHz; coincidence rate ~ 24 Hz; accidental-to-correlated coincidence ratio of 1:88 for a 1 ns coincidence window) or an unbalanced Michelson interferometer. The output of the unbalanced Michelson interferometer is sent to a correlation detector (A2/B2; PerkinElmer SPAD; dark-count rate ~ 450 Hz; background light-count rate ~ 600 Hz; singles rate ~ 67 Hz; coincidence rate ~ 58 Hz). Signals from the detectors (A1/B1/A2/B2) are routed to two high-resolution data acquisition devices (DAQ; PicoQuant PicoHarp run at $\xi = 16$ ps resolution), one DAQ for A1 and A2, and the other DAQ for B1 and B2. The two DAQs are synchronized to each other via a clock signal (with period $T_{sync} = 64$ ns) that is generated by Alice. Alice's and Bob's unbalanced Michelson interferometers both have a path mismatch of $\tau \simeq 10$ ns. Alice's unbalanced Michelson interferometer has an automated 20 nm resolution translation stage in the long arm that she scans as part of the key generation protocol outlined above.

Ideally, for the duration of the QKD process, Alice need only randomly measure the predetermined maximum and minimum locations of the Franson fringes. However, due to phase drifts, for the duration of the experiment Alice's stage is scanned from $c\Delta\tau = 0$ to $c\Delta\tau = 600$ nm $\cong 3\frac{\lambda_p}{2}$ in 50 nm steps with 3 s integral periods. After taking data for a nominal duration of 60 s, Bob sends Alice his Franson event arrival times. Alice uses Bob's Franson event arrival times along with her own

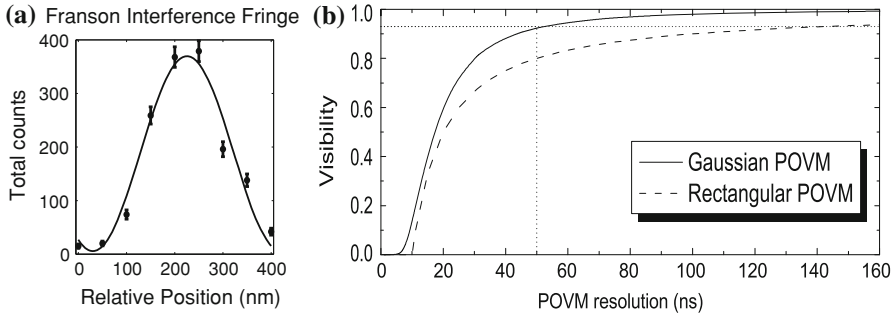


Fig. 6 **a** Franson fringe visibility is measured to be 93%. **b** Franson fringe visibility versus Eve's POVM resolution. The solid curve represents a gaussian POVM, while the dashed curve represents a rectangular-form POVM. A measured visibility of 93% corresponds to a POVM resolution of $\gtrsim 50$ ns, demonstrating security (details in text)

Franson event arrival times to obtain a measured visibility $V = 93 \pm 7\%$ (see Fig. 6a). The error in measured visibility is due to phase instabilities (we require 10 nm stability over 3 m path lengths), which can be improved with an all-fiber setup. The measured visibility is used to estimate the resolution of Eve's POVM in the intercept-resend-type attack discussed previously. Assume that Eve performs a POVM on every photon-pair. A theoretical plot of Franson fringe visibility versus Eve's POVM resolution is shown in Fig. 6b. A gaussian POVM and a rectangular-form POVM are analysed, where the POVM resolution corresponds to four standard deviations for a gaussian POVM (corresponding to 99.99% of the distribution) and the FWHM for the rectangular-form POVM. As seen in Fig. 6b, a measured Franson fringe visibility of $\sim 93\%$ corresponds to Eve's POVM resolution of $\gtrsim 50$ ns. As discussed below, the optimal alphabet obtained in our experiment spans a period of 21 ns. Hence Eve does not gain any detailed information about the key, demonstrating security of the quantum channel. A more rigorous security analysis is beyond the scope of this review, and shall be presented in a later publication. Alice communicates to Bob that the quantum channel is secure and they proceed with the key sifting process of the protocol.

Alice and Bob bin the arrival times of their timing photons. Since the arrival times of each photon is measured with respect to the clock cycle immediately preceding it, the first level of binning is accomplished by Alice and Bob publicly communicating the respective clock cycle, denoted n_a for Alice's clock cycle and n_b for Bob's, during which each photon detection event occurs. Coarse-grained coincidence events are those for which $n_a = n_b$. The simplest form of binning in order to obtain a D -character alphabet involves dividing each 64 ns sync period into D , equally sized bins. Each bin has an equal chance of containing a photon event since a cw-pump is used. Using a bin size of $\sigma = 3\xi = 48$ ps gives us an alphabet of $D = \frac{64\text{ns}}{48\text{ps}} \sim 1278$ characters, i.e. over 10bits per photon. However, the detector electronics jitter has a $1/e^2$ width of 350 ps that results in a very high quantum dit error rate (QDER) of 86%, due to one photon registering in the d 'th bin with Alice while the other photon registers in the $d \pm 1$ 'th bin with Bob. Converting dits to bits, we find that this corresponds to a

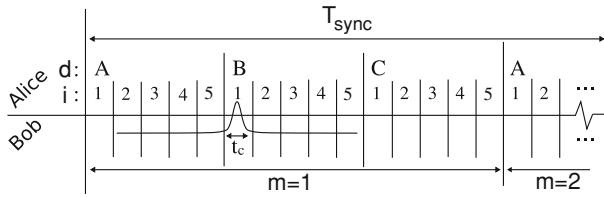


Fig. 7 Example of the binning procedure as outlined in the text. In this example we have used $I = 5$, $M = 2$ and $D = 3$

BER of $\sim 30\%$. Error correction codes can be used to reduce the BER, but are only effective for a raw BER of less than 11% [3].

In order to reduce the raw BER, a process of indexing and redundancy is performed on the bins. Each of the 1278 bins are consecutively indexed from $i = 1$ to $i = I$, with every I consecutive bins representing the same character (see Fig. 7). Alice and Bob publicly announce the index i of their binned photons (but keep the character private). Alice and Bob keep those coarse-grained correlation events that also have the same index, and discard the rest. For example, an index-parameter of $I = 5$ reduces the alphabet to $\frac{1278}{5} = 255$ characters, but also reduces the BER to $\sim 21\%$. This process reduces the BER due to the jitter in the detector electronics, however a sizeable BER remains due to erroneous coincidences that are caused by low collection and detection efficiency, ambient room light, fluorescence in the optics, and dark counts in the detectors.

The BER due to these accidental coincidences can be further reduced by reducing the coarse-grained coincidence window of 64 ns. This is done by dividing the sync period (64 ns) into M , separate periods, denoted n_a^m and $n_b^{m'}$ for Alice and Bob respectively. Alice and Bob publicly announce the sync-division, m , during which a photon is measured, and keep only those coarse-grained coincidences for which $n_a^m = n_b^{m'}$. This reduces the BER due to accidental coincidences, but also reduces the alphabet size $D = 1278$ by a factor M . For example, for $M = 2$, the alphabet size is reduced to 639 characters (assuming $I = 1$). It should be noted that the security of the system, determined by the Franson fringe visibility, is independent of the BER.

By varying σ , I and M , it is possible to find an optimal transmission rate within a desired error bound. As seen in Fig. 8a, the optimal transmission rate for our system, within a BER bound of 5%, corresponds to $\sigma = 240$ ps with 4 bits per photon pair (using $I = 5$ and $M = 3$; not shown). Hence, a real advantage is achieved by incorporating more information per photon pair. Note that this result was obtained for an estimated eavesdropping POVM resolution of $\gtrsim 50$ ns, larger than the $\frac{64}{3} = 21$ ns period of the optimal alphabet, thus demonstrating security. An added benefit of this time-energy system is that this optimization can easily be performed in post-processing, since $\frac{\sigma}{\xi}$, I and M are all computational (as opposed to physical) parameters. Hence, it is very easy to perform a unique optimization for different systems. Further, even if the measured visibility of the Franson fringes is reduced, e.g. due to the presence of an eavesdropper, a new optimization can immediately be performed so as to maintain security. For completeness, an image is encrypted and decrypted using the key obtained for $\sigma = 240$ ps, $I = 5$ and $M = 3$, as shown in Fig. 8b.

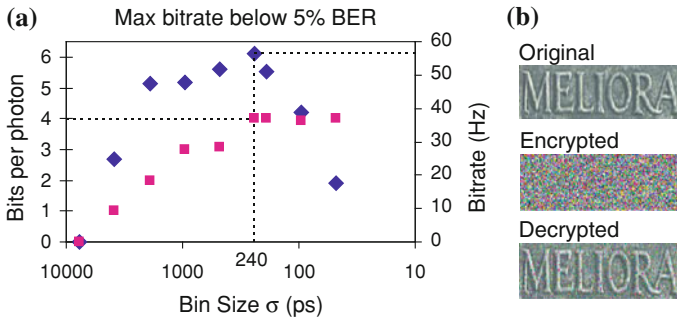


Fig. 8 **a** Diamonds represent optimal bit-rate versus σ (optimized for I and M). Squares represent information per photon pair for each optimization. Overall optimum bit-rate is obtained for $\sigma = 240$ ps, with 4 bits per photon pair. **b** Demonstration of cryptography using optimal key. Image size 32 KB. Key re-used 58 times

We have presented a protocol for large-alphabet QKD using energy-time entangled photons generated by a cw pump, as motivated in [39]. In this QKD protocol, one conjugate basis is used exclusively for key generation while the other conjugate basis is used exclusively for measuring security of the quantum channel. It is possible to maintain secure QKD even in the presence of eavesdropping by monitoring the Franson fringe visibility and re-optimizing $\frac{\sigma}{\xi}$, I and M . We have demonstrated an alphabet of over 10 bits per photon, albeit with a 30% BER. Within a BER bound of 5%, an optimal transmission rate was achieved by using 4 bits per photon. Even larger alphabets can be obtained by using longer sync pulse intervals or higher resolution timing detectors, while the BER would need to be significantly reduced by reducing losses and noise in the system. Energy-time entanglement has previously been demonstrated to be well preserved over large distances in fiber [43, 44], which makes the application of this protocol an exciting prospect for practical QKD.

4 Single-photon image memories

We now turn our attention to potentially useful tools that can be incorporated in the single-photon imaging toolbox. Here, we discuss an all-optical method for delaying or buffering a single-photon image demonstrated by Camacho et al. [27]. In classical image processing, one can change the optical signal into an electronic signal preserving the amplitude and phase of an image via optical homodyning of the image. However, when dealing with a single photon, this cannot be done. Therefore, we seek a method for storing the image that preserves the amplitude and phase of the single-photon image. All-optical methods for delaying images have great potential in signal processing and quantum information. For example, in many digital signal processing applications, amplitude and phase information of an image must be preserved for long periods of time. Electrical conversion of the image can be costly, inaccurate and information is lost in the analogue to digital conversion. Alternatively, one could use a long free space delay line, but diffraction and size limitations impose serious restrictions on the system. A small all-optical buffer in which the phase and amplitudes are

preserved would solve these problems. On the quantum information side, much effort is going toward constructing memories of quantum bits (memories which preserve the wavefunction of a two-state quantum particle). Camacho et al. showed that classical and quantum images could be delayed while still preserving the amplitude and phase information of the image. Further, the image buffer requires no additional laser beams resulting in low background and a high signal to noise ratio in the image reconstruction even at the single-photon level. The transverse images can be delayed by many times the pulse length of the image. The phase stability of the delayed image has almost no dependence on the slow light system, but only the free-space characteristics. This remarkable property leads to stable and high fringe visibility when the delayed image interferes with a local oscillator even if the slow light medium has large spectral or thermal instabilities.

“Slow light” is the name given to a subfield of optics which describes the group velocity (the velocity at which the pulse energy travels) of a pulse in a highly dispersive medium [45,46]. Dispersion means that the index of refraction of a material changes as a function of the frequency of the light and is found in any system which has a spectrally dependent absorption. The group velocity is the slope of the linear term in the dispersion. The effort is to find a medium which has a steep slope, allows a large signal bandwidth, but minimizes the absorption. The slow light medium used in these experiments is a hot Cesium vapor. Delay bandwidth products (the delay of the light signal in the medium multiplied by the bandwidth of the signal) in excess of 50 can be achieved by spectrally tuning the signal between the two hyperfine ground states [47], which have a spectral separation of 9.2 GHz.

While several methods for achieving slow light have been explored, the system discussed here is particularly attractive. For example, most slow light systems, such as electromagnetically induced transparency [48–54], coherent population oscillations [55–57] or spectral hole-burning [58], require additional light fields to prepare the medium. Harris’ group also considered buffering transverse images [48,49], but not at the single-photon level. The use of additional light fields results in transverse spatial inhomogeneities in the group velocity of the medium. In the Cs system used here, the group velocity is the same in all directions. Also, this system has relatively low loss and minimal broadening of the pulse.

A brief overview of some of the most important theoretical elements will be given. A more detailed treatment of the propagation of a Gaussian light pulse through a medium with two widely spaced absorbing Lorentzian optical resonances may be found in [47,59–61]. Assuming two Lorentzian absorption resonances of equal strength, the complex index of refraction may be written as the sum of a free-space term (unity) and two distinct Lorentzian terms:

$$n(\delta) = 1 + \frac{\beta}{2} \left(\frac{1}{-(\delta + \omega_0) - i\gamma} + \frac{1}{-(\delta - \omega_0) - i\gamma} \right) \quad (17)$$

where each resonance has a strength β , a spectral half-width γ , δ is the detuning from the midpoint between the two resonances, and $2\omega_0$ is the separation between the resonances. If the bandwidth of the input pulse is much less than the separation between the resonances, the refractive index may be expanded in a power series and keep only

the first few terms. The real and imaginary parts of the index of refraction, responsible for pulse delay and absorption respectively, may then be written as

$$n' \approx 1 + \frac{\beta}{\omega_0^2} \delta + \frac{\beta}{\omega_0^4} \delta^3 \quad (18)$$

$$n'' \approx \frac{\beta\gamma}{\omega_0^2} + 3\frac{\beta\gamma}{\omega_0^4} \delta^2. \quad (19)$$

It can be seen that $\gamma \frac{dn'}{d\delta} = n''$. This fact can be used to obtain a simple form for the group velocity. Combining this result with $\alpha = 2\omega n''/c$, where α is the optical intensity coefficient of the medium at the pulse carrier frequency, one obtains an approximate group velocity

$$v_g \approx \frac{c}{\omega \frac{dn'}{d\delta}} = \frac{2\gamma}{\alpha}. \quad (20)$$

If the medium is of length L , the resulting pulse delay in the medium relative to that of free space is approximately

$$\tau_g \approx \frac{L}{v_g} = \frac{\alpha L}{2\gamma}. \quad (21)$$

Several points are worth noting. First, the pulse delay is given entirely by the width of the resonances and the optical depth of the medium at the pulse center frequency, and is independent of the separation of the optical resonances. Second, there is no ultimate bandwidth limit on the input pulse, since the input bandwidth is only limited by the frequency separation of the two optical resonances. Third, assuming uniform atomic density the group velocity is homogeneous in the sample. Fourth, while not treated in this analysis, the broadening is relatively small for this system owing to the fact that the dispersive broadening dominates the absorptive broadening. The last point is that the propagation through the medium is a classical effect meaning that its behavior does not change for quantum fields versus classical fields. The place where this system benefits quantum fields is the ultra-low noise background (Fig. 9).

Consider the results for the macroscopic image interference shown in Fig. 10. In Fig. 10a, the Cs cell temperature is set to give 5 ns of delay, which matches the arrival time of the image pulses at the second beamsplitter to that of the reference pulses. The situation in which both pulses arrive at the beamsplitter simultaneously will be referred to as “temporally matched”. The intensity along the two paths is balanced for maximum interference. The phase of the local oscillator is set to give a dark fringe in the center of the image. Several π radians of phase shift across the image can be observed. The only regions that do not experience interference are the image points of the dark patterns of the amplitude mask. Since there is no light in the delayed image at those points, the local oscillator creates a constant background where the dark regions of the amplitude mask are imaged. Hence, at the center of the dark fringe the inverse image is created. An interference visibility of $90 \pm 1\%$ was observed for the temporally

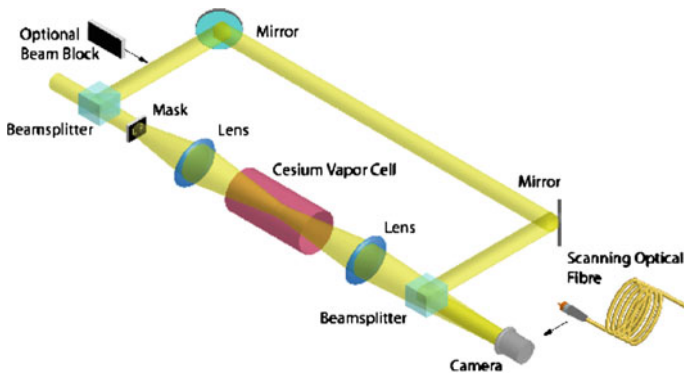


Fig. 9 Experimental setup for the delay of transverse images. Light pulses of 2 ns duration are incident on a 50:50 beamsplitter. The transmitted pulses then pass through an amplitude mask and a 4f imaging system. The transmitted and reflected pulses are recombined at another 50:50 beamsplitter. The transmitted part traverses a path approximately 5 feet shorter than the reflected path, and arrives at the second beamsplitter about 5 ns sooner than the reflected pulse, preventing interference between the two pulses. The temperature of cesium vapor can then be adjusted to give 5 ns of delay, resulting in interference. In the low-light-level experiment, the pulses are attenuated such that each pulse contains on average less than one photon and the reflected path is blocked. A scanning optical fiber is used to collect the photons in the image plane and the photon arrival times recorded using a photon counter with time-to-digital converter

matched pulse regime. The pulses from the two arms of the Mach-Zehnder interferometer are then misaligned in time, so as to arrive at the beamsplitter at different times. This is accomplished by either removing the cell or by tuning the delay of the pulse. In both cases the observed visibility dropped, as seen in Fig. 2b and c, respectively. The images show the same number of phase shifts as the temporally matched pulses but the interference visibility (after balancing the intensity in each arm) is 6% for cell removal and 15% for delay tuning, far lower than the 90% visibility for the temporally matched case. As a note, there is always a small amount of CW light leaking through the electro-optic modulator, which has a 100:1 extinction ratio. The CW light is the primary culprit in giving the nonvanishing interference visibility when the pulses are temporally mismatched. The amount of CW light can be much greater than 1% of the total light since it is constantly “on”, which can lead to a much larger integrated CW signal. In the interference experiment, the CW background is about 5%. The CW background light can be removed by using a camera that is able to gate around a 2 ns window in a fashion similar to that of the low light-level experiment.

The experimental results for the weak field images are shown in Figs. 11, 12, 13. Figure 11a and b show a delayed and non-delayed one-dimensional image (a bar test pattern) where each pulse impinging on the image mask contains, on average, 0.5 photons. The images are measured by scanning an optical fiber in a line across the image plane for a total duration of 36 s. A histogram of the photon arrival times is made for each incremented position of the fiber (an effective pixel) as it scans across the image (shown in Fig. 11c). The measured image is the convolution of the image with the fiber core. For these scans, the laser frequency is set halfway between the optical resonances and the temperature of the cell is set to give 9 ns of delay (shown in red). The process is repeated but with the laser frequency tuned far from either resonance, which

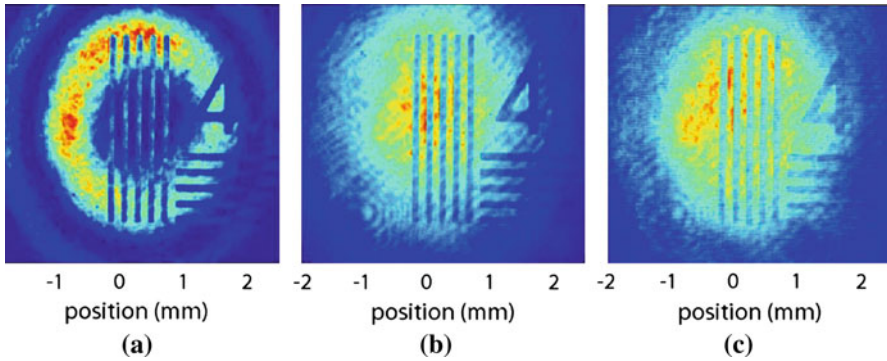


Fig. 10 Interference of a delayed image with a slightly diverging local oscillator. **a** An image (a black pattern of bars and a numeral) delayed by 5 ns interferes with a reference beam and produces a ring pattern superimposed with the image. In the central dark spot, the two beams destructively interfere and cancel one another except in the image, which remains relatively bright. In the ring surrounding the central spot, the two beams constructively interfere and add to create a bright ring except in the image, which remains relatively dim. The succeeding rings alternate between constructive and destructive interference. **b** and **c** show the same superposition of the two beams, but in the absence of slow light. In (**b**), the wavelength of the laser is tuned outside of the dispersive region and in (**c**) the cesium cell is removed. In both cases, no interference between the beams can be seen

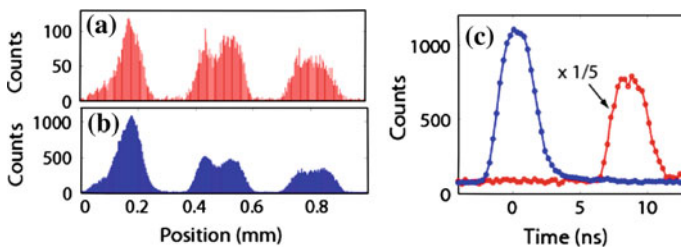


Fig. 11 **a** Delayed and **b** non-delayed one-dimensional low-light-level image with **c** accompanying histograms of photon arrival times. Each pulse contains, on average, 0.5 photons before striking the image mask

gives almost no delay (shown in blue). Approximately 99% of extraneous counts from background light and detector dark counts are removed by constructing the images using only those photons which arrive in a 4 ns time window (out of the entire 330 ns window) centered on the middle of the pulse arrival time distribution. An analysis of the undesirable counts led to an estimate of approximately 2 extraneous counts per spatial bin shown in Fig. 11, which is in good agreement with the image noise.

Figure 12 shows the delay of a two-dimensional image comprised of the letters “UR” representing the researchers’ institution. In this part of the experiment, each pulse contains, on average, 0.8 photons before arriving at the image mask. The image is constructed by raster scanning a fiber across the image plane in a total time of approximately 48 s. The time-binned filtering technique described above was also used to remove background counts from the two-dimensional images. A histogram of the photon arrival times for the two dimensional images of Fig. 12 is shown in Fig. 13,

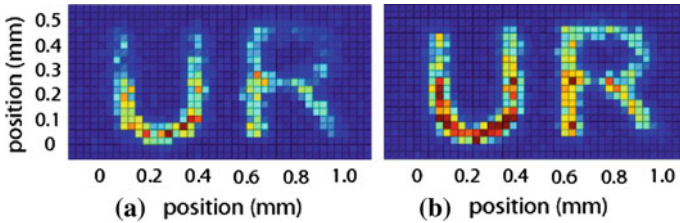
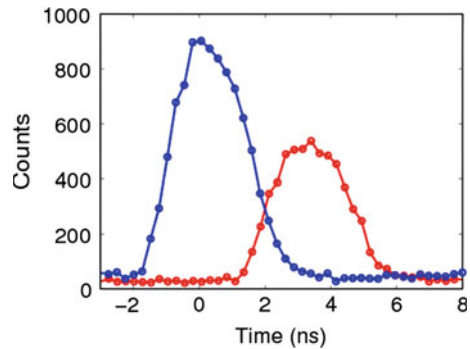


Fig. 12 **a** Delayed and **b** non-delayed two-dimensional low-light-level image. An optical fiber was raster-scanned across a two dimensional image consisting of the letters “UR”. Though attenuated, the delayed imaged shows similar image fidelity and resolution to the non-delayed image. Each pulse contains, on average, 0.8 photons before striking the image mask

Fig. 13 Histogram of photon arrival times showing the delayed (pulse on the right) and non-delayed (pulse on the left) two-dimensional image shown in Fig. 12



showing the delayed image pulses. Even though every photon used to construct the image is delayed by approximately 3 ns, the image is preserved with high fidelity.

A few comments about the results are in order. First, the propagation through the medium is a classical effect, meaning that its behavior does not change in going from classical fields to quantum fields. A formal demonstration of the preservation of quantum fields was not undertaken in the present study. However, the preservation of amplitude and phase as well as the low noise characteristics imply that this system can be an integral part of quantum image buffering. The development of a highly multimode quantum image buffer is a much different goal than that of the preservation of two state systems that have been recently studied (qubits) [53, 54, 62–65]. Second, the homogeneous linewidth of the cesium atoms ultimately determines the upper limit in the absolute delay of our slow light system. However, much narrower resonances could achieve a much larger upper limit of the delay at the expense of the usable signal bandwidth.

A study presented here concentrated on obtaining information about an image carried by a single photon. However, a different scenario has been considered as well. In this scenario, the goal is to obtain an image of a photo-sensitive sample that could be destroyed by a single photon. Such a goal is achievable due to the possibility of a single-photon measurement without interaction.

In a recent work [66], a single-photon-interaction-free measurement has been used to detect an intruder in a sense that it was a single pixel black (intruder is there) or

white (intruder is not there) imaging with no more than a single photon being seen by an intruder. Thus, this approach allows for discrimination between black and white with a high confidence level without photon absorption in the sample. Therefore, a black and white image of any sample could be reconstructed in a statistical fashion after a pixel by pixel scan in a recently developed invisible quantum tripwire modified for scanning microscopy.

References

1. Bennett, C.H., Brassard, G.: Experimental quantum cryptography: the dawn of a new era for quantum cryptography: the experimental prototype is working. *SIGACT News* **20**(4), 78–80 (1989)
2. Ekert, A.K.: Quantum cryptography based on bell's theorem. *Phys. Rev. Lett.* **67**(6), 661–663 (1991)
3. Shor, P.W., Preskill, J.: Simple proof of security of the bb84 quantum key distribution protocol. *Phys. Rev. Lett.* **85**, 441 (2000)
4. Shor, P.W.: In: Proceedings of the 35th Annual Symposium on the Foundations of Computer Science, Los Alamitos, CA. IEEE Computer Society Press, New York (1994)
5. Deutsch, D.: Quantum Computational Networks. *Proc. Roy. Soc. Lond. Math. Phys. Sci.* **425**(1868), 73–90 (1989)
6. Cirac, J.I., Zoller, P.: Quantum computations with cold trapped ions. *Phys. Rev. Lett.* **74**(20), 4091–4094 (1995)
7. Grover, L.K.: Quantum mechanics helps in searching for a needle in a haystack. *Phys. Rev. Lett.* **79**(2), 325–328 (1997)
8. Monroe, C., Meekhof, D.M., King, B.E., Itano, W.M., Wineland, D.J.: Demonstration of a fundamental quantum logic gate. *Phys. Rev. Lett.* **75**(25), 4714–4717 (1995)
9. Kolobov, M.: The spatial behavior of nonclassical light. *Rev. Mod. Phys.* **71**, 1539 (1999)
10. Pierce, E.C.P.J.R., Rodemich, E.R.: The capacity of the photon counting channel. *IEEE Trans. Inf. Theory* **27**, 61 (1981)
11. Shannon, C.E.: The mathematical theory of communication. *Bell Syst. Tech. J.* **27**, 379 (1948)
12. Mair, A., Vaziri, A., Weihs, G., Zeilinger, A.: Entanglement of the orbital angular momentum states of photons. *Nature* **412**, 313 (2001)
13. Molina-Terriza, G., Torres, J.P., Torner, L.: Management of the angular momentum of light: preparation of photons in multidimensional vector states of angular momentum. *Phys. Rev. Lett.* **88**, 013601 (2001)
14. Leach, J., Courtial, J., Skeldon, K., Barnett, S.M., Franke-Arnold, S., Padgett, M.J.: Interferometric methods to measure orbital and spin, or the total angular momentum of a single photon. *Phys. Rev. Lett.* **92**, 013601 (2004)
15. de Riedmatten, H., Marcikic, I., Scarani, V., Tittel, W., Zbinden, H., Gisin, N.: Tailoring photonic entanglement in high-dimensional hilbert spaces. *Phys. Rev. A* **69**, 050304(R) (2004)
16. Barreiro, J.T., Langford, N.K., Peters, N.A., Kwiat, P.G.: Generation of hyperentangled photon pairs. *Phys. Rev. Lett.* **95**, 260501 (2005)
17. Walborn, S.P., Lemelle, D.S., Almeida, M.P., SoutoRibeiro, P.H.: Quantum key distribution with higher-order alphabets using spatially encoded qudits. *Phys. Rev. Lett.* **96**, 090501 (2006)
18. Walther, P., Aspelmeyer, M., Zeilinger, A.: Heralded generation of multiphoton entanglement. *Phys. Rev. A* **75**, 012313 (2007)
19. O'Sullivan-Hale, M.N., Khan, I.A., Boyd, R.W., Howell, J.C.: Pixel entanglement: experimental realization of optically entangled $d=3$ and $d=6$ qudits. *Phys. Rev. Lett.* **94**, 220501 (2005)
20. Ali-Khan, I., Broadbent, C.J., Howell, J.C.: Large-alphabet quantum key distribution using energy-time entangled bipartite states. *Phys. Rev. Lett.* **98**, 060503 (2007)
21. Turin, G.L.: An introduction to matched filters. *IRE Trans. Inf. Theory* **6**, 311 (1960)
22. Goodman, J.: Introduction to Fourier Optics, 3rd edn. Roberts and Company, Greenwood Village, CO (2005)
23. Lugt, A.V.: Signal detection by complex spatial filtering. *IEEE Trans. Inf. Theory* **10**(2), 139 (1964)
24. Horner, J.L., Gianino, P.D.: Phase-only matched filtering. *Appl. Opt.* **23**(6), 812–816 (1984). <http://ao.osa.org/abstract.cfm?URI=ao-23-6-812>
25. Broadbent, C.J., Zerom, P., Shin, H., Howell, J.C., Boyd, R.W.: Discriminating orthogonal single-photon images. *Phys. Rev. A* **79**(3), 033802 (2009)

26. Malik, M., Shin, H., O'Sullivan, M., Zerom, P., Boyd, R.W.: Quantum ghost image identification with correlated photon pairs. *Phys. Rev. Lett.* **104**(16), 163602 (2010)
27. Camacho, R.M., Broadbent, C.J., Ali-Khan, I., Howell, J.C.: All-optical delay of images using slow light. *Phys. Rev. Lett.* **98**, 043902 (2007)
28. Vander Lugt, A.: Coherent optical processing. *Proc. IEEE* **62**, 1300 (1974)
29. Morris, G.M., George, N.: Frequency-plane filtering with an achromatic optical transform. *Opt. Lett.* **5**, 202 (1980)
30. An, X., Psaltis, D., Burr, G.W.: Thermal fixing of 10,000 holograms in linbo3:fe. *Appl. Opt.* **38**(2), 386–393 (1999)
31. Morris, G.M.: Image correlation at low light levels: a computer simulation. *Appl. Opt.* **23**(18), 3152 (1984)
32. Peres, A., Terno, D.R.: Optimal distinction between non-orthogonal quantum states. *J. Phys. A* **31**(34), 7105 (1998)
33. Li, X., Voss, P.L., Chen, J., Sharping, J.E., Kumar, P.: Storage and long-distance distribution of telecommunications-band polarization entanglement generated in an optical fiber. *Opt. Lett.* **30**, 1201 (2005)
34. Neves, L., Lima, G., Gómez, J.G.A., Monken, C.H., Saavedra, C., Pádua, S.: Generation of entangled states of qudits using twin photons. *Phys. Rev. Lett.* **94**, 100501 (2005)
35. Barreiro, J.T., Langford, N.K., Peters, N.A., Kwiat, P.G.: Generation of hyperentangled photon pairs. *Phys. Rev. Lett.* **95**, 260501 (2005)
36. Cerf, N.J., Bourennane, M., Karlsson, A., Gisin, N.: Security of quantum key distribution using d-level systems. *Phys. Rev. Lett.* **88**, 127902 (2002)
37. Nikolopoulos, G.M., Ranade, K.S., Alber, G.: Error tolerance of two-basis quantum-key-distribution protocols using qudits and two-way classical communication. *Phys. Rev. A* **73**, 32325 (2006)
38. Grice, W.P., Walmsley, I. A.: Spectral information and distinguishability in type-ii down-conversion with a broadband pump. *Phys. Rev. A* **56**, 1627 (1997)
39. Ali-Khan, I., Howell, J.C.: Experimental demonstration of high two-photon time-energy entanglement. *Phys. Rev. A* **73**, 031801(R) (2006)
40. Law, C.K., Eberly, J.H.: Analysis and interpretation of high transverse entanglement in optical parametric down conversion. *Phys. Rev. Lett.* **92**, 127903 (2004)
41. Pryde, G.J., O'Brien, J.L., White, A.G., Ralph, T.C., Wiseman, H.M.: Measurement of quantum weak values of photon polarization. *Phys. Rev. Lett.* **94**, 220405 (2005)
42. Franson, J.D.: Bell inequality for position and time. *Phys. Rev. Lett.* **62**, 2205 (1989)
43. Tittel, W., Brendel, J., Zbinden, H., Gisin, N.: Violation of bell inequalities by photons more than 10 km apart. *Phys. Rev. Lett.* **81**, 3563 (1998)
44. Marcikic, I., de Riedmatten, H., Tittel, W., Zbinden, H., Legre, M., Gisin, N.: Distribution of time-bin entangled qubits over 50 km of optical fiber. *Phys. Rev. Lett.* **93**, 180502 (2004)
45. Boyd, R.W., Gauthier, D.J.: In: Wolf, E. (eds.) *Progress in Optics*, vol. 43. Elsevier, Amsterdam, p. 497 (2002)
46. Chiao, R., Milonni, P.: Fast light, slow light. *Opt. Photonics News*, **13**, 26 (2002)
47. Camacho, R.M., Pack, M.V., Howell, J.C.: Low-distortion slow light using two absorption resonances. *Phys. Rev. A* **73**, 063812 (2006)
48. Kasapi, A., Jain, M., Yin, G.Y., Harris, S.E.: Electromagnetically induced transparency: propagation dynamics. *Phys. Rev. Lett.* **74**, 2447 (1995)
49. Jain, M., Merriam, A.J., Kasapi, A., Yin, G.Y., Harris, S.E.: Elimination of optical self-focusing by population trapping. *Phys. Rev. Lett.* **75**(24), 4385–4388 (1995)
50. Kash, M.M., Sautenkov, V.A., Zibrov, A.S., Hollberg, L., Welch, G.R., Lukin, M.D., Rostovtsev, Y., Fry, E.S., Scully, M.O.: Ultraslow group velocity and enhanced nonlinear optical effects in a coherently driven hot atomic gas. *Phys. Rev. Lett.* **82**(26), 5229–5232 (1999)
51. Budker, D., Kimball, D.F., Rochester, S.M., Yashchuk, V.V.: Nonlinear magneto-optics and reduced group velocity of light in atomic vapor with slow ground state relaxation. *Phys. Rev. Lett.* **83**(9), 1767–1770 (1999)
52. Hau, L.V., Harris, S.E., Dutton, Z., Behroozi, C.H.: Light speed reduction to 17 metres per second in an ultracold atomic gas. *Nature* **397**, 594 (1999)
53. Liu, C., Dutton, Z., Behroozi, C.H., Hau, L.V.: Observation of coherent optical information storage in an atomic medium using halted light pulses. *Nature* **409**, 490 (2001)

54. Turukhin, A.V., Sudarshanam, V.S., Shahriar, M.S., Musser, J.A., Ham, B.S., Hemmer, P.R.: Observation of ultraslow and stored light pulses in a solid. *Phys. Rev. Lett.* **88**, 023602 (2002)
55. Bigelow, M.S., Lepeshkin, N.N., Boyd, R.W.: Observation of ultraslow light propagation in a ruby crystal at room temperature. *Phys. Rev. Lett.* **90**(11), 113903 (2003)
56. Zhao, X., Palinginis, P., Pesala, B., Chang-Hasnain, C., Hemmer, P.: Tunable ultraslow light in vertical-cavity surface-emitting laser amplifier. *Opt. Express* **13**(20), 7899–7904 (2005). <http://www.opticsexpress.org/abstract.cfm?URI=oe-13-20-7899>
57. Palinginis, P., Sedgwick, F., Crankshaw, S., Moewe, M., Chang-Hasnain, C.: Room temperature slow light in a quantum-well waveguide via coherent population oscillation. *Opt. Express* **13**(24), 9909–9915 (2005). <http://www.opticsexpress.org/abstract.cfm?URI=oe-13-24-9909>
58. Camacho, R.M., Pack, M.V., Howell, J.C.: Slow light with large fractional delays by spectral hole-burning in rubidium vapor. *Phys. Rev. A* **74**(3), 033801 (2006)
59. Tanaka, H., Niwa, H., Hayami, K., Furue, S., Nakayama, K., Kohmoto, T., Kunitomo, M., Fukuda, Y.: Propagation of optical pulses in a resonantly absorbing medium: observation of negative velocity in rb vapor. *Phys. Rev. A* **68**(5), 053801 (2003)
60. Macke, B., Ségard, B.: Pulse normalization in slow-light media. *Phys. Rev. A* **73**(4), 043802 (2006)
61. Zhu, Z., Gauthier, D.J.: Nearly transparent sbs slow light in an optical fiber. *Opt. Express* **14**(16), 7238–7245 (2006). <http://www.opticsexpress.org/abstract.cfm?URI=oe-14-16-7238>
62. Phillips, D.F., Fleischauer, A., Mair, A., Walsworth, R.L.: Storage of light in atomic vapor. *Phys. Rev. Lett.* **86**, 783 (2001)
63. Kocharovskaya, O., Rostovtsev, Y., Scully, M.O.: Stopping light via hot atoms. *Phys. Rev. Lett.* **86**(4), 628–631 (2001)
64. Bajcsy, M., Zibrov, A.S., Lukin, M.D.: Stationary pulses of light in an atomic medium. *Nature*. **426**, 638 (2003)
65. Yanik, M.F., Suh, W., Wang, Z., Fan, S.: Stopping light in a waveguide with an all-optical analog of electromagnetically induced transparency. *Phys. Rev. Lett.* **93**(23), 233903 (2004)
66. Anisimov, P.M., Lum, D.J., McCracken, S.B., Lee, H., Dowling, J.P.: An invisible quantum tripwire. *New J. Phys.* **12**, 083012 (2010)